# Iron Oxidation at Low Temperature (260–500 °C) in Air and the Effect of Water Vapor

**N. Bertrand · C. Desgranges · D. Poquillon · M. C. Lafont · D. Monceau**

**Abstract** The oxidation of iron has been studied at low temperatures (between 260 and 500 °C) in dry air or air with 2 vol% $H_2O$, in the framework of research on dry corrosion of nuclear waste containers during long-term interim storage. Pure iron is regarded as a model material for low-alloyed steel. Oxidation tests were performed in a thermobalance (up to 250 h) or in a laboratory furnace (up to 1000 h). The oxide scales formed were characterized using SEM-EDX, TEM, XRD, SIMS and EBSD techniques. The parabolic rate constants deduced from micro-balance experiments were found to be in good agreement with the few existing values of the literature. The presence of water vapor in air was found to strongly influence the transitory stages of the kinetics. The entire structure of the oxide scale was composed of an internal duplex magnetite scale made of columnar grains and an external hematite scale made of equiaxed grains. $^{18}O$ tracer experiments performed at 400 °C allowed to propose a growth mechanism of the scale.

**Keywords** Iron · Oxidation · $^{18}O_2$ · Water vapor

## Introduction

In the frame of the 30th of December 1991 French law related to the management of long-lived nuclear wastes, research programs have been performed in different ways. The behaviour of metallic containers in conditions of dry corrosion has therefore been studied considering long-term interim storage [1]. As a matter of fact,

N. Bertrand · C. Desgranges (✉)
CEA, DEN/DPC/SCCME Laboratory of Non Aqueous Corrosion,
91191 Gif-sur-Yvette Cedex, France
e-mail: clara.desgranges@cea.fr

N. Bertrand · D. Poquillon · M. C. Lafont · D. Monceau
CIRIMAT CNRS INPT UPS, ENSIACET, 31077 Toulouse, France

at the beginning of the storage period, because of the heat released by the waste, the container material may reach an initial temperature of 300 °C which will slowly decrease down to 100 °C after about 100 years. During this first stage, dry oxidation will be one of the main degradation modes as no water condensation will occur. After this first stage, for temperatures lower than 100 °C, modification of the material surface by atmospheric or wet corrosion needs to be considered. Low-alloyed steels or carbon steels were the candidate materials for highly radioactive waste containers in long-term interim storage. Even if today, long-term interim storage is no longer the reference way in France, these studies remain pertinent as metallic containers will undergo the same succession of phases prior to the final storage: dry corrosion and atmospheric corrosion. Only few studies dealing with iron and steel oxidation in the temperature range of interest (between 100 and 350 °C) have been reported in the literature. Existing studies below 400 °C have focused on the first stages of oxidation, and no data are available on the effect of water vapor at these temperatures in air or oxygen at atmospheric pressure.

At temperature below 570 °C and at atmospheric pressure, only two iron oxide phases are stable: hematite ($Fe_2O_3$) and magnetite ($Fe_3O_4$). A scale made of an inner magnetite layer thicker than the outer hematite layer is usually reported [2]. The crystallographic structure of the magnetite (inverse spinel) favors cationic transport through the scale. Diffusion in magnetite has been studied by Dieckmann and Schmalzried at high temperatures (900–1400 °C) [3, 4]. Cationic diffusion was found to proceed by an interstitial mechanism at low oxygen partial pressure and via a vacancy mechanism at high oxygen partial pressure. A tracer ($^{55}Fe$) study of Atkinson et al. [5] at 500 °C confirms that the model proposed by Dieckmann et al. is still correct at this low temperature. The growth kinetics of magnetite scales is independent of oxygen pressure in the gas if the oxygen partial pressure is high enough for hematite to be stable [6], which is the case in air. In fact, when a continuous hematite is present in the scale, the concentrations of cationic vacancies at the interfaces are fixed by the equilibria Fe–$Fe_3O_4$ and $Fe_3O_4$–$Fe_2O_3$. Hematite is of rhombohedral structure with low concentration of structural defects. Fe and O have similar diffusion coefficients in hematite with very high activation energy (>400 kJ) [7, 8] and it is not clear which control its growth rate [2, 9, 10]. On one hand, several studies performed at high temperatures [11–15] conclude that hematite grows by dominant inward anion transport, while on the other hand, Francis and Lees [16] who have performed $^{18}O$ tracer experiments at 550 °C incline towards a preferential cationic growth mechanism for the hematite.

In a recent review of iron oxidation in air or oxygen [17], Chen and Yuen underline that below 570 °C oxide microstructure and oxidation kinetics strongly depend on the sample preparation, cold-working or annealing. This phenomenon has been carefully studied by Caplan and co-workers [11, 18, 19]. The oxidation rates of scales developed at 400–550 °C on annealed or electro-polished samples are typically much lower than on hand-polished samples and the parabolic rate constant decreases progressively with time. The scales are also non uniform in thickness; at locations where the scale remains in contact with the iron substrate, it is relatively thick, whereas at locations where the scale–substrate contact is lost, it is very thin. In light of these observations, the decrease of the oxidation kinetics with time is

explained by Caplan et al. by the gradual loss of contact between the scale and the iron substrate [11]. The scales developed at 400–550 °C on cold-worked samples are better adherent to the iron substrate, and more uniform in thickness. They are composed of a thin hematite layer and a thick magnetite layer [18, 19]. Comparison of annealed specimens with specimens of various grounded states show that increasing the cold working results in a more uniform, thicker, and more adherent scale, together with a lower hematite to magnetite thickness ratio [11]. The large population of dislocations on the sample surfaces introduced by cold working provides an effective mechanism for vacancy annihilation, thus reducing the tendency of scale-substrate separation during oxidation at these temperatures. The magnetite layer developed on cold-worked samples is duplex with a fine-grained layer forming at the inner region and a coarser columnar-grained layer at the outer region. The fine-grained layer was believed to form via an oxide-dissociation mechanism, associated with void formation at the scale/iron interface and subsequent void migration along the grain boundaries through the magnetite layer [20, 21]. However no direct evidence that this mechanism participates in the formation of the magnetite duplex layer has been reported. Carbon impurity in iron has been thought to assist the formation of the fine-grained layer and to maintain the adherence between the scale and the iron substrate [9, 19].

The order of appearance of the two oxide phases is not clearly established. According to Chen and Yuen, TEM analysis made by Goswami in 1965 [22] revealed that the hematite layer appears at the end of the oxidation process in the following stages: Fe → $Fe_3O_4$ → α-$Fe_2O_3$. On the contrary, Davies et al. published in 1954 results indicating that the hematite layer appeared first and that magnetite could nucleate only after a few hours and spread locally below the hematite oxide film [23].

For low-alloyed steels or carbon steels, the scale formed during the dry oxidation stage of a long-term interim storage is “rapidly” thick enough to apply the Wagner’s model [24] and to assume parabolic oxidation kinetics. Considering that the hematite/magnetite thickness ratio is rather small, scale growth kinetics can be estimated using the Wagner’s model and the diffusion coefficient of cations estimated by Dieckmann and Schmalzried in magnetite [3, 4]. However, this led Atkinson et al. [5] to calculate a value of $2 \times 10^{-14}$ $cm^2$ $s^{-1}$ for the parabolic rate constant at 500 °C which is two orders of magnitude smaller than the experimental value. The large contribution of short-circuits diffusion at low temperature might explain this discrepancy.

Another way to perform a long term prediction of oxidation kinetics consists in extrapolations based on $k_p$ values measured experimentally. This leads to an estimated iron oxide thickness of 60 μm after 100 years at 300 °C [25]. But this prediction relies on the hypothesis of a unique mechanism controlling the oxide growth throughout the duration considered. For long-term interim storage, more experimental data are required to understand effects such as influence of experimental conditions (temperature, atmosphere), evolution of parameters controlling transport in the scale, scales microstructure evolution and effects occurring at interfaces or in the metal. Several phenomena are expected to play a major role in the oxidation rate at low temperature. First, diffusion along grain boundaries can be the major transport mechanism at low temperature [26]. In order to model scale

growth over long time period, it is essential to characterize the nature, morphology and microstructure of the scales and particular care has to be taken to determine grain sizes of the pertinent oxides. Moreover, partial interfacial control of oxidation kinetics may also be expected [27]. Zheludkevich et al. [28] have studied the influence of oxygen dissociation on the iron oxidation rate: It was found negligible at 300–800 °C. However, in ambient air, the water vapor present in the atmosphere could affect interfacial reactions [29]. So a careful analysis of long term oxidation kinetics is required.

The present study intends to explore the temperature range between 260 and 500 °C, for which few data are available in the literature. The paper is divided in two main parts. The study of the growth kinetics and microstructure of scales formed on pure iron in wet air (2 vol% $H_2O$) is reported in the first part. Particular attention is devoted to the effect of the humidity in the atmosphere. The second part relies on to the investigation of the oxide scale growth mechanism by the means of $^{18}O$ marker experiments followed by SIMS analysis.

## Materials and Experimental Procedure

All samples were machined from the same ARMCO pure iron sheet. The composition of this material is given in Table 1. These specimens ($30 \times 10 \times 2$ mm$^3$) were mechanically grounded using 1200 grit SiC paper, and then cleaned in alcohol, dried and left for about 3 days in ambient atmosphere. The microstructure of all samples is composed of α phase grains. The typical grain size is around 30 μm.

Thermogravimetric analyses during oxidation treatments were performed in a SETARAM TAG 24S thermobalance. The accuracy of this thermobalance measuring mass variation is about 1 μg at all temperatures. Furnace temperatures were controlled using Pt/Pt–Rh 10% thermocouples and regulated within ±1 °C. The oxidation tests were performed between 260 and 400 °C in three different oxidizing atmospheres: (1) Dry synthetic air (21% $O_2$, 79% $N_2$), (2) a mixture of dry air and $H_2O$ vapor (2 vol%) prepared through a SETARAM Wetsys device, (3) a mixture of dry air and $H_2O$ vapor (2 vol%) obtained by air double bubbling in deionized water. The value of 2 vol% $H_2O$ vapor in volume was chosen because it is representative of interim storage conditions. When the specimens were hung in the thermobalance, a primary vacuum was created in the furnaces before filling with He (99.9995%) during heating (10 °C/min) followed by 20 min of thermal stabilization once the target temperature was reached. During these stages, the residual oxygen pressure in He is relatively high (about $10^{-3}$ atm) and the atmosphere can not reduce the passive layer formed during the 3 days exposition of the sample in ambient air at room temperature. Once the temperature was stabilized, the oxidizing atmosphere was introduced in the furnace

**Table 1** Composition of studied material (Fe ARMCO) (wt%)

| | C | Mn | Si | S | P | Ni | Cr | Mo | Cu | Sn | Al | N |
|---|---|---|---|---|---|---|---|---|---|---|---|---|
| Fe ARMCO | 0.001 | 0.05 | 0.01 | 0.003 | 0.004 | 0.019 | 0.013 | 0.001 | 0.005 | 0.002 | 0.001 | 0.003 |

with a flow rate of 2.2 L/h (corresponding to a gas velocity of $10^{-3}$ m $s^{-1}$). After the high temperature oxidation stage, cooling was carried out under a flow of He. The thermocouple of the oven for TGA is verified by procedure based on fusion temperature of different pure metals.

A second set of samples was oxidized in a classic laboratory furnace which allows the exposure of several samples to a controlled atmosphere at the same time. These isothermal oxidation tests have been performed at 300 and 400 °C with durations varying from 42 min to 1000 h. The temperature of the oven is controlled at ±2 °C and verified with a standard thermocouple. Specimens were introduced into the quartz tube in a pre-heated furnace and exposed to a continuous flow of 8 or 15 L/h of oxidizing gas (corresponding respectively to a gas velocity of $10^{-3}$ and $2 \times 10^{-3}$ m $s^{-1}$). Two oxidizing atmospheres were used: (1) dry synthetic air (21% $O_2$, 79% $N_2$) and (2) a mixture of dry air and $H_2O$ vapor (2 vol%) obtained by air double bubbling in deionized water. All samples were weighed before and after exposure.

After oxidation, all the specimens were observed with a scanning electron microscope (SEM LEO 1450 VP). Subsequently, the oxide scales were fractured and observed with a FEG–SEM (LEO 1525). Some oxide scales were also characterized by X-ray diffraction (XRD) at room temperature. The measurements were performed on a Phillips equipment (X'Pert MPD Panalytical S.A with incidence angles of 1° or 6°) using Co K$\alpha$ radiation ($\lambda k\alpha 1 = 1.78897$ Å). The diffraction patterns were obtained in the $2\Theta$ range of 20–100° with a step size of 0.025°. The oxide phase was identified with data files in the JCPDS index. Some of the samples were investigated using transmission electron microscopy (TEM). TEM observations of the thin oxide layers were performed using a JEOL JEM 2010 microscope operating at 200 kV equipped with a "TRACOR" EDX spectrometer. For TEM observations, cross-sections were prepared: Samples were cut into two thin slices normal to the oxide/substrate interface with a diamond wire saw. The slices were glued together, oxide-to-oxide, and embedded in a 3 mm diameter brass tube with an epoxy resin. After curing, the tube was sectioned into approximately 300 μm discs which were polished on the two faces and dimpled before ion-milling to transparency with a precision ion beam polishing system (GATAN PIPS). Additionally, a cross-section sample was examined using a FEG–SEM Supra 55 operated at low vacuum (20 Pa) and equipped with an "HKL Technologie" (Channel 5) EBSD system with a high sensitivity "Nordlys II" detector. For $^{18}O$ tracer experiments, secondary ion mass spectrometry (SIMS) was used to investigate the sequence of oxide scale formation and to precise the localization of $^{16}O$ and $^{18}O$ in the scale. The apparatus was a CAMECA IMS 4F6. Oxidized sampled were gold coated and primary beam of $Cs^+$ ions was used for pulverization in the SIMS.

## Results

### Kinetics of Scale Growth

Long-term thermogravimetric measurements (about 250 h) have been performed at 260, 300, 400, and 500 °C in dry or wet (2 vol% $H_2O$) air as explained previously.

The parabolic rate constant ($k_p$) was calculated from mass gain measurement by using the most general expression for parabolic kinetics:

$$t = a + b\,\Delta m + c(\Delta m)^2 \quad (1)$$

where $\Delta m$ is the mass-gain per unit area (mg $cm^{-2}$) and t the time (s). In Eq. 1, the coefficient c is equal to the reciprocal of the parabolic rate constant $k_p$ ($mg^2$ $cm^{-4}$ $s^{-1}$), independent of the initial conditions for integration of the rate equation, and independent of a possible partial interface control of oxidation kinetics [30]. Equation 1 could be fitted to local set of (t, $\Delta m$) data to evaluate if a stable regime of parabolic kinetics was reached. Then, Eq. 1 was fitted to the entire range of parabolic kinetics to obtain a global and more precise value of $k_p$. Table 2 gives the $k_p$ values obtained. These values are compared with those from the literature in the Arrhenius plot presented in Fig. 1. Parabolic rate constants determined in this work are in good agreement with data available in the literature [5, 11, 18, 19, 23, 31–36]. The effect of cold working on oxidation of iron at 400–650 °C [5] is well known and special care was taken during the present study to prepare the specimens with the same polishing. The activation energy of the oxidation process in wet air (2 vol% $H_2O$) found in the present work is 151 ±30 kJ/mol. This value can be compared with data of Sakai et al. (149 ±17 kJ/mol) in air [34] and Graham et al. (134 kJ/mol) at low oxygen pressure ($1.7 \times 10^{-5}$ bar) [35].

**Table 2** Parabolic rate constant $k_p$ ($mg^2$ $cm^{-4}$ $s^{-1}$), values determined from the stable stage of oxidation

| | 260 °C | 300 °C | 400 °C | 500 °C |
|---|---|---|---|---|
| Synthetic dry air | | $4.1 \times 10^{-9}$ | $3.1 \times 10^{-6}$ | |
| Syn. air + 2 vol% $H_2O$ (SETARAM Westys system) | | $1.3 \times 10^{-8}$ | $2.7 \times 10^{-7}$ | |
| Syn. air + 2 vol% $H_2O$ (bubbling) | $8.1 \times 10^{-10}$ | | $3.4 \times 10^{-7}$ | $2.7 \times 10^{-5}$ |

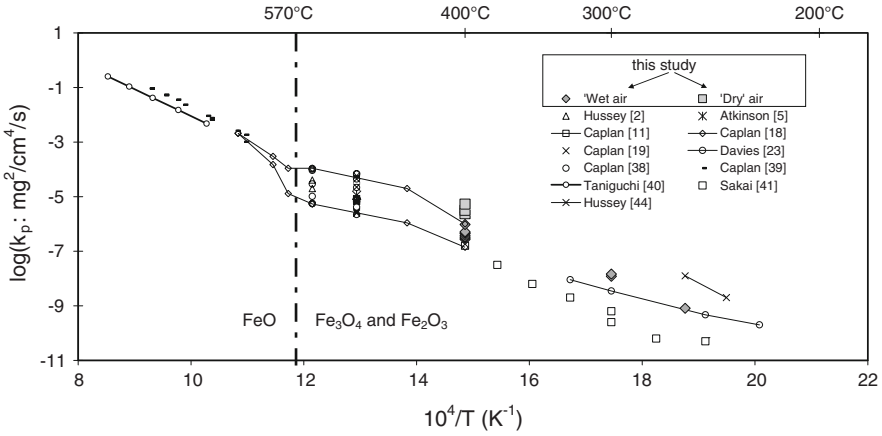


**Fig. 1** Oxidation kinetics obtained in this study (Table 2) compared with literature data: Arrhenius plot

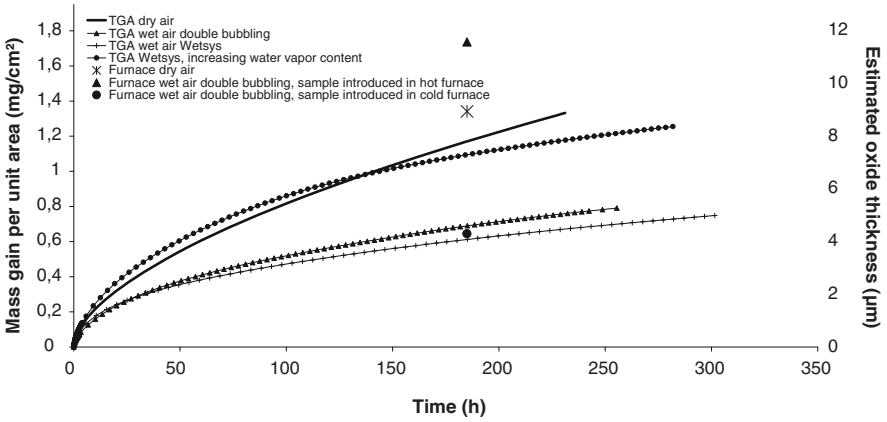


**Fig. 2** Mass gain curves obtained during isothermal oxidation at 400 °C under different atmospheres (gas flow $2 \times 10^{-3}$ m $s^{-1}$). Comparison between TGA experiments and laboratory furnace oxidations

Oxidation performed in laboratory furnace in dry air confirmed these oxidation kinetics (e.g. Fig. 2 for 400 °C), whereas the results are more complicated for wet air as explained below.

*Influence of Water Vapor Content in Air*

In order to investigate the influence of humidity of the atmosphere on oxidation kinetics, tests have been repeated in different atmospheres (dry and wet air) and with different gas flow rates at 400 °C in the laboratory furnace.

For dry air, the mass gains obtained were comparable with TGA data whatever the gas flow (from 8 to 15 L/h). For wet air (2 vol% $H_2O$) obtained by dry air bubbling, the values of the mass gain obtained were also not sensitive to the gas flow rate (from 8 to 15 L/h) but the mass gains obtained for all the tests carried out in the laboratory furnace were larger than the value obtained during TGA analysis in the thermobalance, as shown in Fig. 2. Since thermocouples of both TGA and furnace have been verified with appropriate procedure, this discrepancy could not be due to a temperature deviation. The different heating conditions were supposed to explain differences of oxidation kinetics. Indeed, for the oxidation tests carried out in the laboratory furnace, samples were introduced into the hot furnace in the oxidizing atmosphere, whereas during TGA analysis samples were heated in He atmosphere. This difference does not affect the results obtained in dry air but significantly changes the results for wet air. To validate this explanation, because the SETARAM TAG 24S thermobalance does not allow sample introduction into hot furnace, the sample was heated in the thermobalance in dry air with an increasing amount of $H_2O$ vapor in order to reach 2 vol% at 400 °C and to avoid any condensation at lower temperature. This procedure resulted in an initial mass gain larger that when the specimen was heated in He (Fig. 2). After 250 h, the net mass gain remains slightly smaller than that obtained for samples oxidized in the same conditions but in the laboratory furnace. This difference may be due to the

different heating rates and to lower water content during the beginning of heating in the thermobalance. Despite of these differences in initial oxidation kinetics, the stabilized $k_p$ were comparable for samples oxidized in wet air in the thermobalance, irrespective of whether the heating was done in He or wet air.

In summary, 2 vol% $H_2O$ in air decreases the mass gain at 400 °C. The oxidizing conditions during heating (water vapor and heating rate) change the mass gain during the first 150 h without affecting the $k_p$ values after stabilization (Table 2). Caplan et al. noticed similar result: oxidation rate of iron at 500 °C were reduced when oxygen flow was applied to the pre-heated hot sample compared to the case where cold samples were introduced into the reaction zone with hot oxygen [19]. Graham and Hussey [36] and Hussey et al. [37] also notice a change in the oxidation rate of iron at 200 and 300 °C. They attributed this change to the presence of a thin initial oxide film which, first, accelerates kinetics because of short-circuits present in this initial scale and, second, lowers oxidation rate when oxide detaches from the substrate. In our study, scale detachment was never observed. So, the initial increase in oxidation kinetics could rather be explained by a higher nucleation rate due to more efficient $H_2O$ dissociation on a sample colder than the flowing gas. An increase of nucleation rate leads to a smaller grain size in the oxide scale and, thus, to a higher density of grain boundaries acting as short-circuit diffusion paths. After this initial stage, grain growth decreases the short-circuit density and this could explain why the oxidation kinetics were comparable after 100 h whatever the initial oxidation step.

At 300 °C, mass gain data were found to be similar in dry air and wet air [38].

## Oxide Scale Microstructure

This part shows how water vapor, temperature and oxidation duration affect the microstructure of the oxide scale.

### *Surface Scale Morphologies*

The observation of the surface of the specimen oxidized at 400 °C reveals large differences depending on the nature of the atmosphere (dry air or air + 2 vol% $H_2O$). The surface of sample oxidized in dry air is covered with small rounded crystallites and shows an open porosity with a complete absence of whiskers (Fig. 3). On the other hand, the surfaces of the samples oxidized in wet air are covered with whiskers or platelets. Platelet morphology depends on temperature. Figure 4 shows the evolution of the surface morphology of scales formed at temperatures between 300 and 500 °C in air + 2 vol% $H_2O$. On samples oxidized at 300 and 400 °C in wet air for 260 h, many whiskers appear at the surface. Electron diffraction patterns were obtained during TEM observations on a whisker formed after 260 h at 300 °C and revealed that it was hematite ($\alpha$-$Fe_2O_3$) [39]. At 300 °C, the whiskers are longer and thinner than at 400 °C and furthermore, some areas have a low density of platelets. In [40], Voss et al. are focused on in the whiskers and platelets of hematite at higher temperature (600–800 °C) and with low partial pressure of oxygen. They showed the existence of a tunnel along the axis of

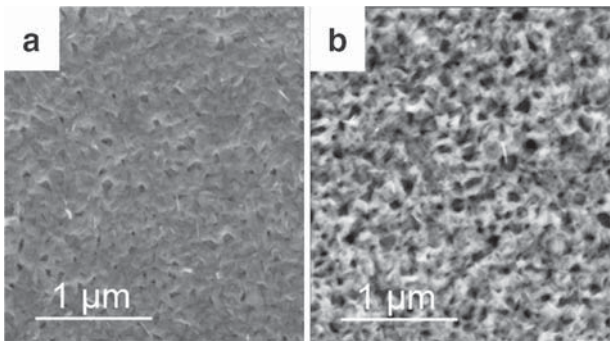


**Fig. 3** FEG–SEM observations of the oxide surface morphology formed in dry air at 400 °C for 232 h: **a** SE in lens; **b** SE

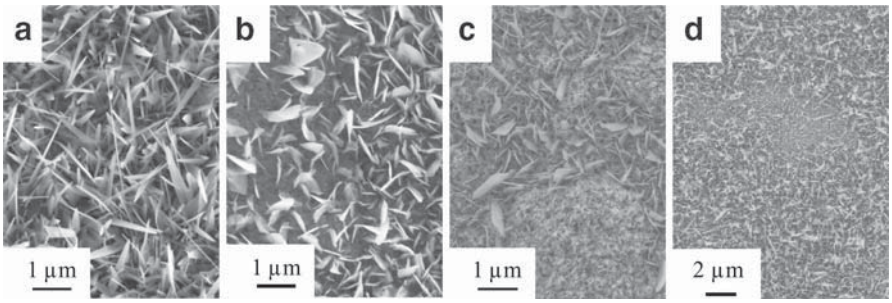


**Fig. 4** Iron oxide surface morphology formed in air + 2 vol% $H_2O$ under different conditions (temperature, exposure period): **a** 300 °C, 260 h; **b** 400 °C, 260 h; **c** 500 °C, 28 h; **d** 300 °C, 1000 h

these needles and platelets, allowing fast surface diffusion of cations along this tunnel. At the highest temperatures, they have also noticed the presence of twin boundaries enhancing the lateral diffusion and explaining the flattened aspect of surface crystallites. The mechanism that they have proposed makes it possible to explain the differences in shape between whiskers and platelets as a function of temperature. In the case of the present study, a competition between whisker nucleation and growth must occur. Indeed, at 300 °C nucleation seems to prevail and many very long whiskers were observed, with an enhanced effect of the diffusion of cations in the whiskers. At 400 °C, the lateral diffusion becomes larger possibly assisted by the presence of twin boundaries. Moreover, Raynaud and Rapp [41] highlighted that the whiskers and the platelets were longer in the presence of steam, in the case of NiO. They explained this phenomenon by the fact that the $H_2O$ molecule dissociates faster than the $O_2$ molecule. Indeed, the limiting stage of the growth of the surface crystallites can be the dissociation of the oxidizing gas molecule since central screw dislocation in the needle allows a very fast diffusion of cations. In the present study, whiskers and platelets were never observed when oxidation was carried out in dry air. This phenomenon can be compared with the results of Hänsel et al. [42] for the oxidation of Cr at high temperature, where the

authors explained that if there was much oxygen present in the oxidizing atmosphere, it was adsorbed preferentially and covered the surface preventing any local variation due to dissociation with the water molecule.

In addition, the morphology of the surface of the oxide layer formed in wet air at 300 °C evolves between 260 and 1000 h (Fig. 4a, d). Indeed, after 1000 h, some zones are whisker depleted and present rounded crystallites, as if the whiskers have been incorporated in the dense equiaxed external hematite layer (Fig. 4d). The same observation can be done at higher temperature for shorter oxidation times. For example, a sample oxidized 28 h at 500 °C in wet air (Fig. 4c) also exhibits the two different morphologies.

In [41], Raynaud and Rapp have also observed (for NiO) that whiskers have disappeared after long oxidation duration. They explained this phenomenon by the blocking of the fast diffusion channels inside the whiskers. Then, surface diffusion only remains active and flattens the surface. The thickening of NiO platelets and their progressive embedding in the oxide scale have also been described in details by Peraldi et al. [43].

*Inner Scale Microstructure*

Some observations of fractured cross-sections of iron oxides formed at 400 °C during 260 h in dry or wet air are given in Fig. 5. The oxide scale is composed of three different microstructures. At the metal/oxide interface, rather a thin layer of small columnar grains was observed. Above it, a layer of coarser columnar grains occupies a large part of the oxide thickness and at the oxide/gas interface a very thin layer of very small equiaxed grains is observed. At 300, 400 and 500 °C, whatever the atmosphere, the oxide scale is always composed of such three layers. Nevertheless, these three-layered scales exhibit three distinct microstructures. Table 3 summarizes the microstructural characteristics of each of the three layers for the different specimens. Both specimens oxidized at 300 and 400 °C for 260 h

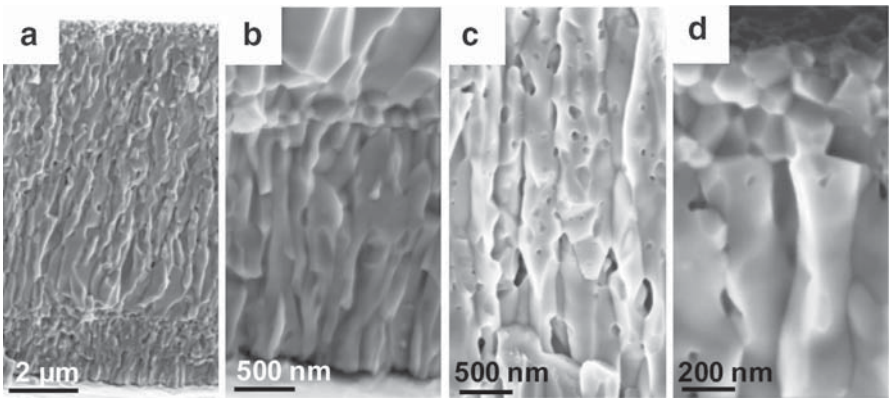


**Fig. 5** Fractured cross-section of oxide scale formed at 400 °C during 260 h during TGA test observed with the FEG–SEM: **a** overall picture, air + 2 vol% $H_2O$; **b** internal part, air + 2 vol% $H_2O$; **c** middle layer of the scale, dry air; **d** external part, dry air

**Table 3** Microstructural characteristics of iron oxide scales formed during different oxidation treatments

| | 300 °C<br>260 h<br>air + 2 vol% $H_2O$ | 400 °C<br>260 h<br>air + 2 vol% $H_2O$ | 400 °C<br>260 h<br>dry air | 500 °C<br>28 h<br>air + 2 vol% $H_2O$ |
|---|---|---|---|---|
| Surface morphology | Whiskers | Platelets | Round crystallites | Whiskers + round crystallites |
| Outer layer of the scale | Fine grains | Equiaxed grains d $\sim$ 100 nm | Equiaxed grains d $\sim$ 100 nm | Equiaxed grains $100 < d < 300$ nm |
| Middle layer of the scale | Small columnar grains d $\sim$ 100 nm | Columnar grains d $\sim$ 300–600 nm<br>Porosity in the upper half part | Columnar grains d $\sim$ 400 nm<br>Porosity in the upper half part | Columnar grains d $\sim$ 500 nm<br>Porosity in the upper half part |
| Inner layer of the scale | Fine grains | Fine columnar grains | Fine columnar grains | Fine columnar grains |

Where d is the typical size for the equiaxed grains, typical width size for columnar grains

show columnar grains in the middle of their scales. Even if there is a large difference between the scale thickness (1 μm vs. 14 μm), the microstructures are similar, but with a typical grain size of 100 nm at 300 °C and of about 200 nm at 400 °C. Tests performed at 400 and 500 °C allow the comparison of the microstructures of scales of the same thickness despite the different temperatures, following the idea developed in [43]. In this case, the outer layer is thin (300–500 nm) and composed of equiaxed grains. The middle layer is made of columnar grains of about 400 nm diameter showing porosities of about 100 nm in the upper part of this intermediate layer. This is illustrated in Fig. 5c. The inner scale is composed of smaller columnar grains than the middle layer (Fig. 5b).

A separation between the inner and middle layers was observed several times on samples oxidized at 300 and 400 °C. The origin of this phenomenon has not been investigated but it does not seem to be due to the sample preparation prior to SEM observations. Indeed, it was observed on fractured specimen as well as on some polished cross-sections. Scale separation could happen during furnace cooling or be due to growth stress during oxide scale growth. An alternative explanation could be an accumulation of vacancies at this interface.

Figure 6 illustrates the morphologies of a scale formed in wet air at 400 °C during 305 h. At 400 °C, the internal microstructure of the scales observed after fracture does not depend on water vapor [38]. Low content of water vapor (2 vol%) seems to affect only the surface morphology of the oxide scale.

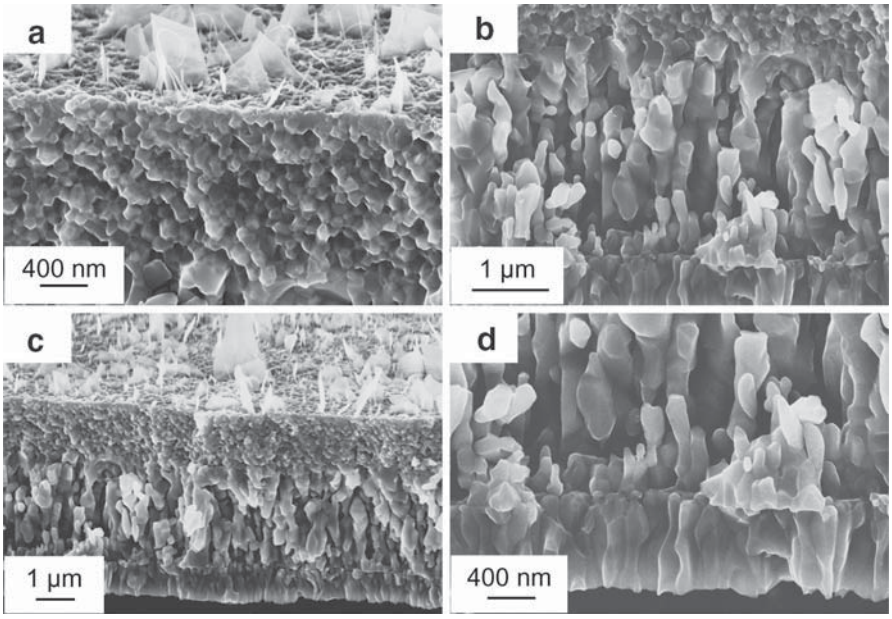


**Fig. 6** FEG–SEM observations of the fractured cross-sections of the oxide scale for a sample oxidized at 400 °C during 305 h in wet air (Wetsys 2 vol% $H_2O$) (the total scale thickness estimated from mass gain is 5.3 μm): **a** external layer of very fine equiaxed grains; **b** external magnetite layer with columnar grains; **c** whole oxide scale; **d** internal magnetite layer with small columnar grains

In order to study the microstructure of thin iron oxide scales, samples were oxidized at 400 °C for shorter durations and at lower temperatures (260 and 300 °C). Then cross-sections were prepared for TEM observations. The three-layered arrangement of the microstructure was systematically observed for all the tests carried out in this study for temperatures from 260 to 400 °C and for oxidation duration ranging from 28 to 300 h. The thinnest oxide scale observed was about 200 nm thick (Fig. 7). However the sub-layers were too thin to be determined if the grains were columnar or equiaxed. The microstructure of the external part of the oxide scale formed at 260 °C was to fine to observe its details. It seems to be amorphous (Fig. 7b). When the thickness was sufficient to identify its microstructure, a thin layer of columnar grains was always found at the metal/oxide interface, followed by a thick layer of coarser columnar grains and finally, by thin layer of very small equiaxed grains present next to the oxide/gas interface (Fig. 8).

X-ray diffraction analyses were carried out on several samples, with two incidence angles (1° and 6°). These XRD results indicate that a hematite layer is located over a magnetite layer. Considering the microstructure of scales and the data from previous studies it seems reasonable that the two inner layers made of columnar grains were layers of magnetite ($Fe_3O_4$) and that the outer layer made of equiaxed grains was hematite ($\alpha$-$Fe_2O_3$). These results are in good agreement with the work carried out by Hussey et al. [2]. For the oxidation of iron at 550 °C in $O_2$, these authors observed a duplex layer made of columnar grains under a layer of equiaxed grains. The thickness of the layers they have studied varies from 2 to 38 μm varying as a function of the exposure time (from 0.1 to 120 h). However, in [2], no local analysis had been carried out in order to unambiguously identify which phase corresponds to each layer. This was achieved in the present study thanks to TEM and EBSD techniques, as detailed in the next paragraph.

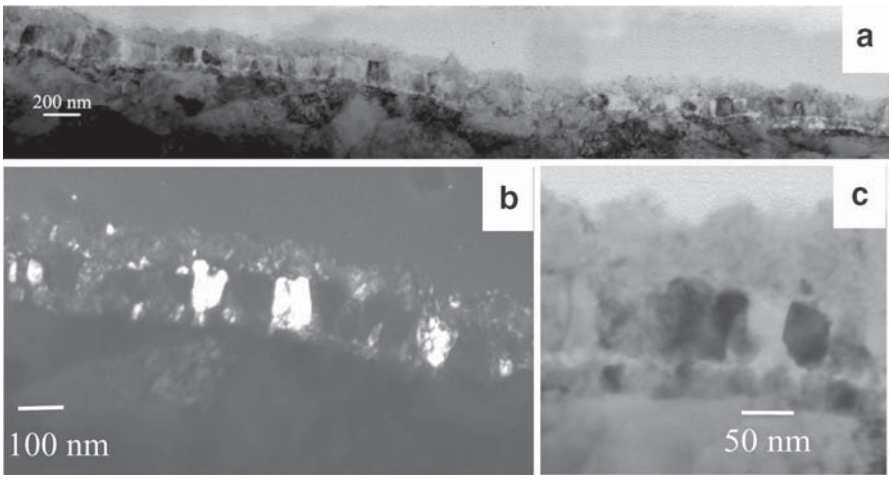


**Fig. 7** TEM observations of the oxide scale formed during TGA exposure at 260 °C for 96 h in air + 2 vol% $H_2O$: **a** assembly of images allowing checking the homogeneity of the oxide scale on a few microns; **b** the three zones of distinct microstructures are highlighted in dark field; **c** the grains of the middle of the scale are columnar whereas the external layer seems to be amorphous

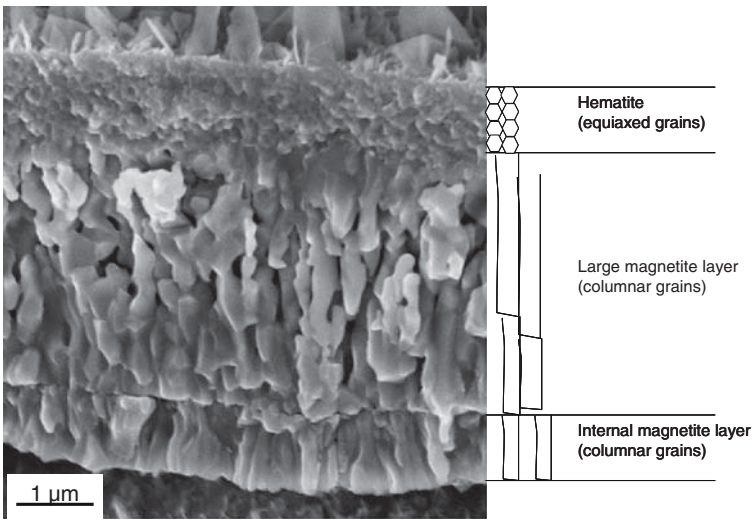


**Fig. 8** Oxide scale formed on pure iron at 400 °C, 256 h in wet air (2 vol% $H_2O$, double bubbling): three sub-layers (Similar microstructure was observed between 260 and 400 °C)

*Local Identification of the Phases and Texture*

In order to identify the different phases of the oxide layer, a cross-section of the oxidized sample have been prepared for local electronic diffraction in the TEM. In order to measure patterns on individual grains, it was necessary to work on an oxide scale with relatively coarse grains. Thus, a sample with an oxide scale about 5 µm thick was prepared to this purpose in the thermobalance (400 °C, 145 h, air + 2 vol% $H_2O$). A cross-section was extracted from this sample for TEM observation. Figure 9 summarizes the TEM observations and the phase identifications. This figure shows the electron transparent oxide on its entire 5 µm thickness; the two layers of columnar grains were separated by the resin used for the mounting. The diffraction patterns obtained on the columnar grains layers correspond to magnetite. The diffraction patterns obtained on the small equiaxed grains layer correspond to hematite. These TEM observations confirm the nature of the three different layers observed in the specimens of this study, that is to say the existence of a duplex layer of magnetite on iron oxidized at low temperature (260–400 °C). The central magnetite layer is thicker and present coarser grains than the internal magnetite layer. The third layer, the thin external one, is composed of equiaxed hematite grains.

Furthermore, some analyses using Electron Back-Scattered Diffraction (EBSD) in a FEG–SEM operated at low vacuum have been carried out on a sample oxidized 120 h at 400 °C in laboratory furnace, in a flow of wet air (2 vol% $H_2O$). The oxide scale thickness was approximately 10 µm. EBSD analyses allow characterization of the nature of the phases and determination of the orientation of the grains. An EBSD map of 166 × 698 points was performed with a step of 30 nm. In Fig. 10a

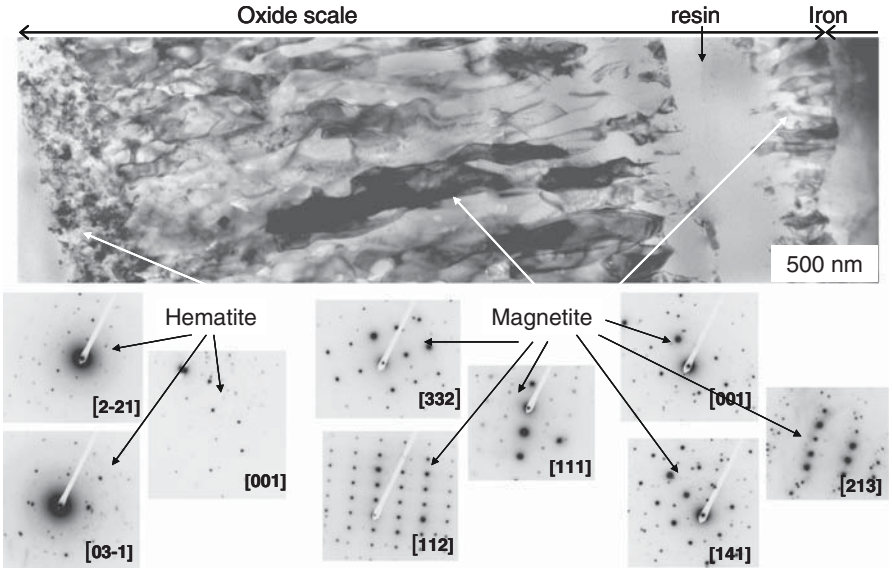


**Fig. 9** Local electron diffraction with the TEM on an oxide scale (400 °C, 145 h, air + 2 vol% $H_2O$): two layers of columnar grains form a duplex layer of magnetite, the equiaxed grains are identified as hematite

reconstructed from this Electron Back-Scatter Diffraction Pattern (EBSP), grains identified as BCC Fe are colored in white, whereas grains identified as the magnetite phase are shown in pattern quality grey scale (the brighter the pixel, the better the EBSP quality). As grain boundaries correspond to a bad quality EBSP (superimposition of two patterns), this map evidences the microstructure of the scale. The duplex structure of magnetite layer is confirmed. The hematite equiaxed grains in the external layer were too small to be analyzed by EBSD.

No epitaxial relationship between the substrate and the oxide scale has been evidenced in the analyzed zone but a texture was revealed in the magnetite scale. The contoured inverse pole figure (Fig. 10b) shows that a large amount of grains with alignment of a $\langle 113 \rangle$ axis with the normal direction of the sample (Y). It is also illustrated on the map of the Fig. 10c which shows in grey the magnetite grains with alignment of a $\langle 113 \rangle$ axis with the normal of the sample: 22% of the points are within 15° of this texture.

*Evolution of the Microstructure of the Scale with Time and Water Content*

To understand the mechanisms occurring during this complex oxide scale formation, the evolution of the thickness of each of the three layers of the oxide scale have been studied. To evaluate the thickness of the oxide layers, ten measurements have been systematically made all along the fractured scale observed by FEG–SEM for each one of the three distinct layers composing the scale. The total oxide thickness was also compared with the oxide thickness calculated using the mass gain data. The

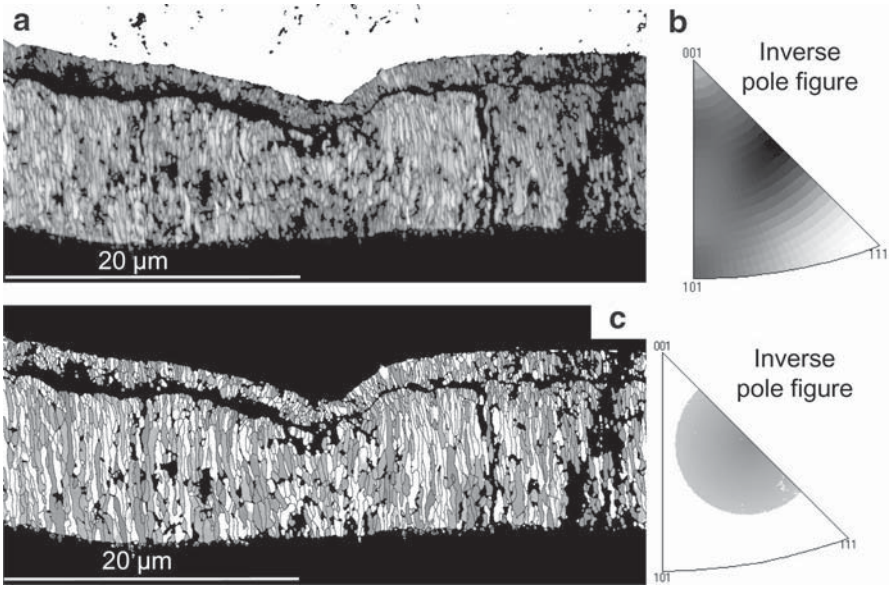


**Fig. 10** EBSD of the cross-section of a sample oxidized at 400 °C during 120 h in a flow of wet air (2 vol% $H_2O$): **a** map showing in white the points that were indexed as bcc iron and in pattern quality grey scale (the brighter the pixel, the better the EBSD quality) the points indexed as magnetite (The points that were not indexed (including the resin) are marked in black); **b** contoured inverse pole figure in a grey scale (the darker the corresponding orientation, the higher the density) showing that a large amount of grains with alignment of a ⟨113⟩ axis with the normal direction of the sample (Y); **c** map showing in grey the magnetite grains with alignment within 15° of a ⟨113⟩ axis with the normal of the sample, and in white the other magnetite grains. Black lines are high angle grain boundaries (>10°) in the magnetite phase

**Table 4** Oxide scale thickness resulting for exposures at 400 °C for 120, 210 and 310 h, under wet air

| Oxidation duration (h): | | 120 | 210 | 310 |
|---|---|---|---|---|
| Entire scale | Average (µm) | 13.5 (100%) | 15.7 (100%) | 14.4 (100%) |
| | Standard deviation (µm) | 0.5 | 1.1 | 1.3 |
| Internal Magnetite | Average (µm) | 2.0 (15%) | 2.4 (15%) | 2.3 (16%) |
| | Standard deviation (µm) | 0.2 | 0.3 | 0.2 |
| External Magnetite | Average (µm) | 11.1 (82%) | 12.6 (81%) | 11.4 (79%) |
| | Standard deviation (µm) | 0.3 | 0.9 | 1.4 |
| Hematite | Average (µm) | 0.41 (3%) | 0.51 (3%) | 0.69 (5%) |
| | Standard deviation (µm) | 0.12 | 0.13 | 0.19 |

values calculated from the mass gain were always slightly lower than the calculated values from SEM micrographs. This can be explained by the presence of porosity in the oxide scale. Table 4 summarized the results obtained for oxidation tests performed at 400 °C in wet air in the laboratory furnace. In the range of oxidation duration investigated (from 120 to 310 h) the relative proportion of each layer does

**Table 5** Oxide scale thickness after oxidation in thermobalance at 400 °C

| | Oxidation duration (h) | Whole scale thickness (μm) | Internal magnetite μm (%) | External magnetite μm (%) | Hematite μm (%) |
|---|---|---|---|---|---|
| Dry air | 232 | 11.9 | 1.5 (13%) | 10 (84%) | 0.35 (3%) |
| Air + 2 vol% $H_2O$ (SETARAM Westys) | 305 | 4.9 | 0.86 (18%) | 2.8 (57%) | 1.2 (25%) |
| Air + 2 vol% $H_2O$ (bubbling) | 265 | 5.3 | 1.3 (24%) | 2.9 (55%) | 1.1 (21%) |

not change with time. The internal magnetite layer occupies 15% of the oxide scale, the external hematite layer occupies 4% and the central layer (external layer of the duplex magnetite layer) occupies the largest part (81%).

As explained before, the way heating is carried out influences the oxide thickness. Oxidation tests were therefore carried out in the thermobalance in order to explore the differences between scales formed in dry and wet air. Results are given in Table 5. First of all, the oxide scale formed in dry air is thicker than the scale formed in wet air. This point is consistent with oxidation kinetics data. Moreover, the oxide layer appeared more compact in dry air and a large amount of porosity was observed in the scale formed in wet air (Figs. 4c and 5b and [38]). The proportion of the internal part of the duplex magnetite layer is the same ($\approx$15%) but a large difference was observed for the external hematite layer. In dry air, the hematite layer accounts for only 3% of the total thickness of the oxide scale whereas in wet air it corresponds to more than 20%. This result will be discussed in the last part of this paper. In the case of samples oxidized in wet air in the thermobalance, the proportion of hematite is greater than for samples oxidized in laboratory furnaces. This has been attributed to the difference in the way the samples are heated. These quantitative evaluations of the proportion of each layer in the oxide scale are in good agreement with all the observations carried out in this study, from 260 to 400 °C, in dry and wet air and for oxide scale thickness ranging from 200 nm (95 h at 260 °C) to 15 μm (310 h at 400 °C). For given oxidation conditions: (1) the proportion of each layer does not change with time; (2) on the thickest scales observed (about 10 μm) obtained at 400 and 500 °C, the proportions of the different layers also seem to be independent of temperature; (3) the hematite layer is thicker and the middle magnetite layer thinner, when formed in wet air than in dry air.

## Identification of the Scale Growth Mechanisms

The microstructure of the iron oxide scale remains unchanged (nature and proportion of each layer) over a large range of temperature and of oxidation duration. At this point of the study, further investigations were needed to identify the mechanisms involved in the formation of each of these three layers. Basu and Halloran [44] have shown that the comprehension of growth mechanisms in an

oxide scale can be deduced from the $^{18}O$ profile obtained during oxidation carried out successively in $^{16}O_2$ and $^{18}O_2$. The shape of the $^{18}O$ profile depends on the ratio between cationic and anionic transport through the scale and depends on the diffusivity of the species in the volume and along grain boundaries.

*Experimental Procedure*

The samples were first oxidized in $^{16}O_2$ at a pressure of 1.2 bar. Then a $1.5 \times 10^{-6}$ mbar vacuum was created in the furnace, and $^{18}O_2$ gas at a pressure of 1.2 bar was introduced in the furnace for a given duration before the natural cooling of the furnace. Each experiment was carried out with two samples in order to duplicate the results. The size of the samples was $15 \times 10 \times 2$ mm$^3$. A 3 mm hole was bored in each sample in order to hang it. The temperature chosen for these experiments was 400 °C, but the temperature measured in the furnace by the thermocouple below the sample was between 415 and 420 °C. The total duration of the oxidation was fixed at 8 h. Three series of experiments have been carried out with three different sequences: 4 h in $^{16}O_2$ then 4 h in $^{18}O_2$; 1 h 40 min in $^{16}O_2$ then 6 h 20 in $^{18}O_2$; 50 min in $^{16}O_2$ then 7 h 10 min in $^{18}O_2$. An additional experiment was performed in $^{16}O_2$ only during 5 h followed by a secondary vacuum in order to check that the establishment of a secondary vacuum did not modify the oxide scale microstructure when compared to the previous experiment in dry air at 1.0 bar. This additional experiment was also used to determine the natural isotopic ratio $^{16}O/^{18}O$ of the oxide layer. The thickness of the oxide scale formed during these tests has been estimated by weighing and was in good agreement with the tests carried out previously in synthetic air. After SEM observations, secondary ion mass spectrometry (SIMS) was used to investigate the localization of $^{16}O$ and $^{18}O$ in the scale.

*Results of Tracer Experiments*

Figure 11 shows the concentration profiles obtained by SIMS analysis of the positive ions for the sample oxidized 4 h in $^{16}O_2$ and then 4 h in $^{18}O_2$. The maximum quantity of $^{18}O$ is located at the oxide/gas interface. The concentration then decreases in the middle of the oxide layer but increases again at the metal/oxide interface. The location of this interface was determined using the point of inflection of the Fe concentration profile. Concerning the $^{16}O$ profile, the entire peak concentration is located inside the scale. Hence, the totality of the oxide scale formed during the initial oxidation of 4 h in $^{16}O_2$ is in the middle of the final layer obtained after 8 h of oxidation. The entire hematite layer and also the external part of the magnetite layer are composed of $^{18}O$. The two other series of tests performed in this study (1 h 40 min in $^{16}O_2$ then 6 h 20 min in $^{18}O_2$; 50 min in $^{16}O_2$ then 7 h 10 min in $^{18}O_2$) allowed a longer oxidation in $^{18}O_2$ and the internal and the external maxima of the $^{18}O$ concentration profiles were again present but not as well separated as in the first test. These $^{16}O_2/^{18}O_2$ experimental results are detailed in another forthcoming publication.

The $^{16}O_2/^{18}O_2$ experiments prove that the oxygen necessary for the growth of the internal part of the magnetite duplex layer comes from the oxidizing gas and not

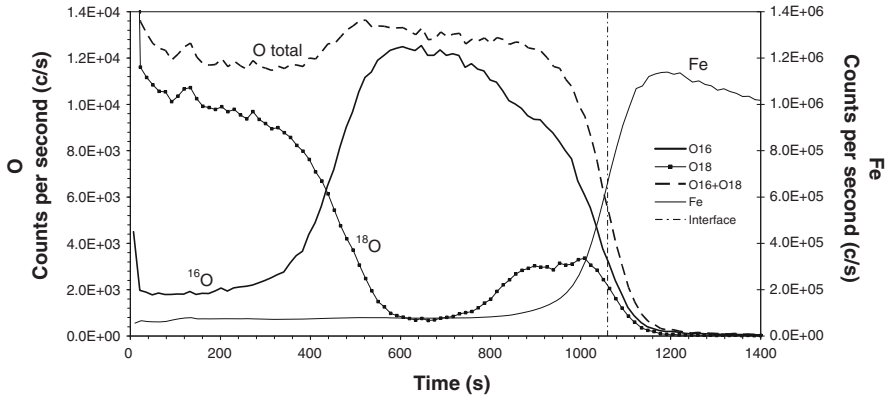


**Fig. 11** The concentration in depth profiles (counts per second) of $^{16}O$, $^{18}O$ and Fe as a function of depth (in time of sputtering) for a sample oxidized 4 h in $^{16}O_2$ then 4 h in $^{18}O_2$. The total thickness of the scale is estimated as equal to 1.65 μm

from the dissociation of the external part of the magnetite duplex layer. Oxygen diffuses through the oxide scale towards the metal/oxide interface via short-circuits such as grain boundaries, pores surface, or porosity in the form of ionized $O^{2-}$ or molecular $O_2$. In addition, the external growth of the magnetite layer is maintained by the reduction of the hematite at the hematite/magnetite interface. This result is inferred from the presence of a single peak of $^{16}O$ within the layer. There is no direct contribution of oxidizing gas molecules for the cationic growth of magnetite.

The $^{16}O_2/^{18}O_2$ experiment also gives information on the growth mechanisms of the hematite layer. Two points can be deduced from the fact that there was no remaining $^{16}O$ at the oxide/gas interface. First, the whole hematite layer formed in $^{16}O_2$ during the first stage of the oxidizing treatment was reduced to magnetite. Second, the hematite layer grows at the external surface by outward cation diffusion. Otherwise the external part of the hematite layer would be composed of $^{16}O$. This mechanism is consistent with the presence of whiskers and platelets in the case of oxidation carried out in wet air.

Experiments of successive oxidations on pure iron have already been carried out by Atkinson and Taylor [45] (in $CO_2/C^{18}O_2$). These authors did not notice any transport of oxygen through the oxide scale. However, their $^{18}O$ profile was not flat at the iron/oxide interface and even if it was not very well marked, an $^{18}O$ concentration bump was present near this interface. Finally, even if the conclusions of Atkinson and Taylor are not the same as those of the present work, the distribution profiles of $^{18}O$ are in good agreement (Fig. 4a, b of [45]) with those of this study. Moreover, $^{18}O$ profiles obtained in our study indicated that oxygen diffusion in the oxide scale is faster than that calculated from diffusion data available in the literature [46, 47]. This result implies a mechanism of formation for the magnetite duplex-scale which differs from the dissociation mechanism initially proposed by Mrowec for the formation of the duplex layers [48], and considered by several authors studying iron oxidation [20, 21].

## Model of Oxide Scale Growth

Considering the obtained results, it is possible to propose a mechanism for the growth of the oxides scales formed on iron at low temperature (260–400 °C) in dry or wet air (2 vol% $H_2O$). $^{18}O_2$ experiments proved that the external part of the duplex magnetite layer and the hematite layer grow by cation outward diffusion. Cation vacancies diffuse inward in the magnetite layer. For hematite, the diffusion mechanism involves more likely interstitial cations (*n*-type semi-conductor). As suggested by Goursat and Smeltzer [8], diffusion of cationic species across the hematite could also proceed via grain boundaries. This hypothesis is supported by the low activation energies for hematite growth in comparison with the very high activation energies reported for the bulk diffusion of iron in hematite [7, 8]. The rate controlling step of the overall oxidation rate is the cationic diffusion in the external magnetite layer. Indeed, this layer is the thickest of the three layers and has the largest grain size. Then, this layer controls the amount of diffusion of oxygen through its short-circuit diffusion paths and then controls the growth kinetics of the internal magnetite layer. $^{18}O_2$ experiments proved that hematite is reduced to magnetite at the hematite/magnetite interface. The cation flux across the external magnetite layer controls the amount of hematite reduction at the hematite/magnetite interface. Hence, the thickness and growth rate of the hematite layer is partly controlled by the growth of the magnetite layer, and partly by the diffusion of cations through hematite.

Following this overall mechanism, the growth rates of the three oxide layers depend on each other. This explains why the proportion of the ratio of oxide layers thicknesses remains constant during scale growth in a given atmosphere.

As cationic diffusion in magnetite is controlling the overall scale growth rate and because the oxygen activity is fixed at both magnetite interfaces, growth kinetics should not depend on the oxidizing atmosphere, excepted through the slight contribution of the external hematite layer growth. Nevertheless, it was observed that water vapor reduces the oxidation kinetics.

The observed effect of $H_2O$ is to increase the thickness of the hematite layer and to decrease the thickness of the external magnetite layer, when compared to dry air oxidation. These observations are consistent with the proposed overall mechanism if $H_2O$ decreases the diffusion in the magnetite layer. Indeed, this would lead to a thinner magnetite layer but also to lower kinetics of reduction of hematite and therefore a thicker hematite layer.

Two possible explanations for the water effect on diffusion in magnetite are given below. The first one relies on the presence of pores in the external layer of magnetite. In wet air, the transport of $H_2O$ through the magnetite towards the metal/oxide interface could generate a discharge of hydrogen in the oxide scale. This phenomenon provides an explanation for the large amount of porosity observed in scales formed in the wet atmosphere. On the other hand, Maruyama et al. [49] explained the presence of porosity inside the magnetite scale in terms of the oxygen chemical potential distribution in the scale, which is dependant on gas composition. For those authors, the presence of voids in a specific part of the scale corresponds to a peak in the divergence of the oxygen flux, which appears to be due to a drastic

change in the oxygen chemical potential distribution in the scale at this particular position. Whatever the origin of this porosity, it could act as barrier for cationic diffusion. Nevertheless, as explained before, a grain boundary mechanism is likely for cations diffusion in magnetite at these low temperatures and the effect of pores on diffusion is not obvious.

A second possible explanation for the effect of water vapor is that hematite formation is partially due to water dissociation. Then, the released hydrogen may diffuse into the oxide scale and decrease the cationic vacancy concentration in magnetite at the hematite/magnetite interface. Indeed, $H_2$ could form $OH^-$ interstitials in magnetite, which should be compensated by cationic vacancies annihilation in order to conserve cationic/anionic sites number ratio. This reaction corresponds to a decrease of sites number and then it is more likely to occur at the hematite/magnetite interface. Then, the driving force for cations transport through the magnetite layer would be lower.

The proposed mechanisms for the growth of each sub-layer of the oxide scale are summarized on Fig. 12, where the hematite needles and platelets were not represented. The latter grow in wet air by rapid diffusion of the cations along a central dislocation to their tips as described by Voss et al. [40]. In the present study, some SEM observations at high magnification are compatible with the existence such a rapid diffusion path along the axis of these needles and platelets (Fig. 13). The limiting step of their fast growth is then the dissociation of the oxidizing gas molecule at the needles and platelets' tip. For temperatures higher than the temperatures used in this study, their length decreases and this can be explained by the considerable lateral diffusion of cations under these conditions. For the very long durations of oxidation, the whiskers and the platelets are incorporated in the oxide scale and disappear.

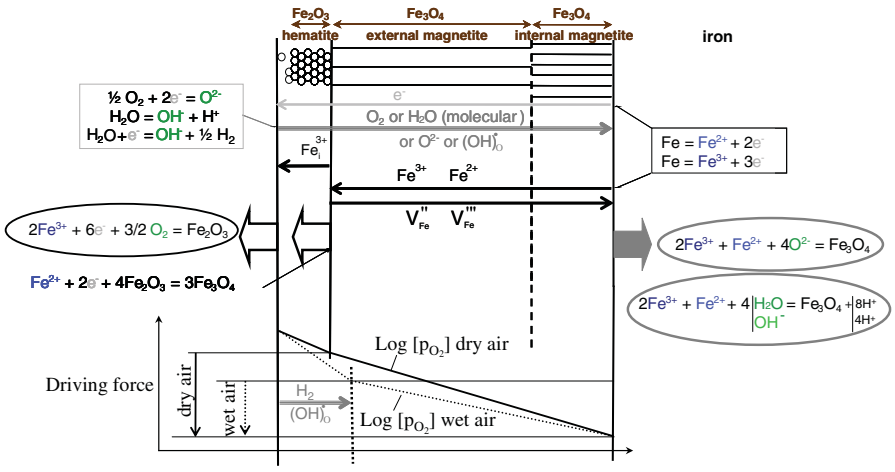


**Fig. 12** Proposed mechanism for the oxidation of iron at low temperature (260–400 °C) in dry air or air containing 2 vol% $H_2O$. *Upper part*: schematic description of the three layered scale (the thickness ratio of layers is not respected; see text for values); *Middle part*: transport of different species in the scale (cationic transport in black, anionic transport in grey) and corresponding oxide reaction formation and interface motion; *Bottom part*: comparison of driving forces in dry air and wet air

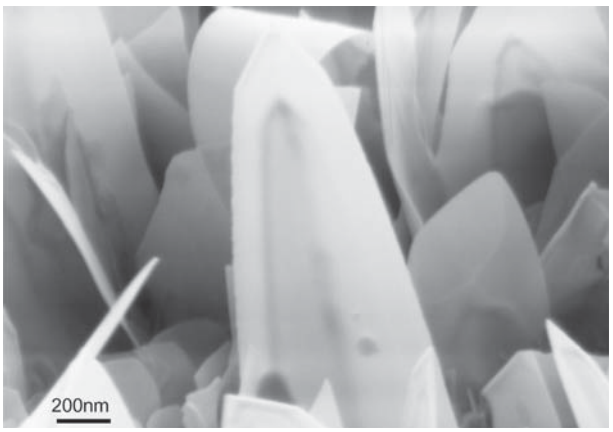


**Fig. 13** High magnification FEG–SEM observation of the needles on the top of iron oxide scale formed at 400 °C, 256 h under wet air (2 vol% $H_2O$)

## Conclusions

The objective of this study was to determine the mechanism of growth of iron oxide at low temperature in order to be able to identify the elementary mechanisms that should be taken into account in a numerical model for the prediction of the behaviour of nuclear waste containers which will be submitted to dry corrosion prior to atmospheric corrosion conditions [50]. Isothermal oxidation of pure iron samples was carried out in dry air and wet air with 2 vol% $H_2O$ in the range of temperatures from 260 to 400 °C. This temperature range is of interest for the "dry" corrosion stage during interim storage. The oxidation kinetics appears to be parabolic and faster in dry air than in wet air at 400 °C. Observations of the oxide scales formed show the presence of three layers: a thin layer of magnetite with columnar grains at the metal/oxide interface, a thick layer of magnetite with coarse and columnar grains in the middle of the scale, and a thin layer of hematite made of equiaxed grains at the gas/oxide interface. Moreover, when oxidation is carried out in wet air, the surface of the oxide scale is covered with needles (or platelets at 400 °C) of hematite. This complex morphology of the iron oxide scale was observed even for the thinnest layers, i.e. down to a 140 nm thick scale. The proportions of these three layers were constant with oxidation time (120–310 h). The thick magnetite layer in the middle of the scale is more porous than other layers. Sequential oxidation of pure iron has been carried out in $^{16}O_2/^{18}O_2$ in order to determine the oxide scale growth mechanisms. Results confirm that the magnetite grows mainly by outward cation transport but evidence of inward transport of oxygen to the internal interface via short-circuits (grain boundaries, porosities,…) in the form of molecular $O_2$ or ionized $O^{2-}$ is also found. Hence, the origin of the duplex structure of the magnetite is explained by a new mechanism.

A model has been proposed for the overall growth of the oxide scale which is consistent with all the preceding observations. According to this model, the rate

controlling step of the oxidation kinetics is the cation diffusion in the external magnetite layer. The thickness of this layer controls the amount of inward diffusion of oxygen through its short-circuits and then controls the growth kinetics of the internal magnetite layer. The outward cation flux across the external magnetite layer also controls the amount of hematite reduction at the hematite/magnetite interface, and then controls partly the thickness of the hematite layer which grows by cationic diffusion at the oxide/gas interface. The lower oxidation rate in case of wet air may be attributed to two mechanisms decreasing the diffusion in the external magnetite layer. The first one is the formation of porosity in magnetite which could be due to hydrogen production within the scale because of $OH^-$ (or $H_2O$) reaction with iron at the internal duplex layer. The presence of porosity acting as diffusion obstacles would lower diffusion in the magnetite scale. The preferred second explanation is related to the released hydrogen resulting from reduction of water molecules at the scale surface. Hydrogen diffuses fast into the oxide scale and can form $OH^-$ interstitials at the hematite/magnetite interface, compensated by cationic vacancies annihilation. Then, the driving force for cations transport across the magnetite layer would be decreased.

The results of this study also show that diffusion via grain boundaries must be considered when modeling iron oxide scale growth at low temperature over long duration. Thus, data concerning the grain size of each layer of the scale that are reported in this paper thanks to TEM observations and EBSD analysis are of particular interest to build a predictive model for dry corrosion phase of nuclear waste containers prior to their final storage.

**Acknowledgments** The authors gratefully acknowledge Claude Armand (INSA Toulouse) for SIMS Analysis, Patrick Bonaillie and Sylvie Poissonnet (CEA) for SEM observations, Rikke Ollemann (HKL Technology) and Daniel Galy (Synergie4) for EBSD analysis, Fabrice Legendre and Sébastien Cabessut (CEA) for $^{16}O_2/^{18}O_2$ oxidation.

## References

1. M. Butez, G. Bordier, X. Vitart, and I. Hablot, *Clefs CEA (CEA Publications, France, 2005)* **53**, 26 (2005).
2. R. J. Hussey, G. I. Sproule, D. Caplan, and M. J. Graham, *Oxidation of Metals* **11**, 65 (1977).
3. R. Dieckmann and H. Schmalzried, *Berichte der Bunsen-Gesellschaft* **81**, 344 (1977).
4. R. Dieckmann and H. Schmalzried, *Berichte der Bunsen-Gesellschaft* **81**, 414 (1977).
5. A. Atkinson, M. L. O'Dwyer, and R. I. Taylor, *Journal of Materials Science* **18**, 2371 (1983).
6. H. Sakai, T. Tsuji, and K. Naito, *Journal of Nuclear Science and Technology* **21**, 844 (1984).
7. R. Lindner, *Arkiv for Kemi* **4**, 381 (1952).
8. A. G. Goursat and W. W. Smeltzer, *Oxidation of Metals* **6**, 101 (1973).
9. D. A. Channing and M. J. Graham, *Corrosion Science* **12**, 271 (1972).
10. N. Birks and G. H. Meier, *Introduction to High Temperature Oxidation of Metals* (Edward Arnold Ltd., 1983), p. 198.
11. D. Caplan and M. Cohen, *Corrosion Science* **3**, 139 (1963).
12. W. E. Boggs, R. H. Kachik, and G. E. Pellissier, *Journal of the Electrochemical Society* **112**, 539 (1965).
13. L. Himmel, R. F. Mehl, and C. E. Birchenall, *Transaction of American Institute of Mining and Metallurgical Engineers* **197**, 827 (1953).

14. M. H. Davies, M. T. Simnad, and C. E. Birchenall, *JOM-Journal of Minerals Metals & Materials Society* **3**, 889 (1951).
15. M. H. Davies, M. T. Simnad, and C. E. Birchenall, *Transaction of American Institute of Mining and Metallurgical Engineers* **197**, 1250 (1953).
16. R. Francis and D. G. Lees, *Corrosion Science* **16**, 847 (1976).
17. R. Y. Chen and W. Y. D. Yuen, *Oxidation of Metals* **59**, 433 (2003).
18. D. Caplan and M. J. Cohen, *Corrosion Science* **6**, 321 (1966).
19. D. Caplan, M. J. Graham, and M. Cohen, *Corrosion Science* **10**, 1 (1970).
20. R. F. Tylecote and T. E. Mitchell, *Journal of the Iron and Steel Institute* **196**, 445 (1960).
21. A. Atkinson, *Reviews of Modern Physics* **57**, 437 (1985).
22. A. Goswami, *Indian Journal of Chemistry* **3**, 385 (1965).
23. D. E. Davies, U. R. Evans, and J. N. Agar, *Proceedings of the Royal Society of London Series A* **225**, 443 (1954).
24. C. Wagner, *Corrosion Science* **9**, 91(1969).
25. C. Desgranges, K. Abbas, and A. Terlain, *Prediction of Long Term Corrosion Behavior in Nuclear Waste Systems* (European Federation of Corrosion 36, 2003), p. 194.
26. A. Atkinson, R. I. Taylor, and A. E. Hughes, *Philosophical Magazine A* **45**, 823 (1982).
27. C. Wagner, *Corrosion Science* **10**, 641 (1970).
28. M. L. Zheludkevich, A. G. Gusakov, A. G. Voropaev, A. A. Vecher, K. A. Yasakau, and M. G. S. Ferreira, *Oxidation of Metals* **62**, 223 (2004).
29. A. Galerie, Y. Wouters, and M. Caillet, *Materials Science Forum* **369–382**, 231 (2001).
30. D. Monceau and B. Pieraggi, *Oxidation of Metals* **50**, 477 (1998).
31. D. Caplan, G. I. Sproule, and R. J. Hussey, *Corrosion Science* **10**, 9 (1970).
32. D. Caplan, R. J. Hussey, G. I. Sproule, and M. J. Graham, *Corrosion Science* **21**, 689 (1981).
33. S. Taniguchi and D. L. Carpenter, *Corrosion Science* **19**, 15 (1979).
34. H. Sakai, T. Tsuji, and K. Naito, *Journal of Nuclear Science and Technology* **22**, 158 (1985).
35. M. J. Graham, S. I. Ali, and M. Cohen, *Journal of the Electrochemical Society* **117**, 513 (1970).
36. M. J. Graham and R. J. Hussey, *Oxidation of Metals* **15**, 407 (1981).
37. R. J. Hussey, D. Caplan, and M. J. Graham, *Oxidation of Metals* **15**, 421 (1981).
38. N. Bertrand, PhD thesis, Institut National Polytechnique de Toulouse, France (2006).
39. N. Bertrand, C. Desgranges, D. Gauvain, D. Monceau, and D. Poquillon, *Materials Science Forum* **461–464**, 591 (2004).
40. D. A. Voss, E. P. Butler, and T. E. Mitchell, *Metallurgical and Materials Transactions A: Physical Metallurgy and Materials Science* **13**, 929 (1982).
41. G. M. Raynaud and R. A. Rapp, *Oxidation of Metals* **21**, 89 (1984).
42. M. Hänsel, W. J. Quadakkers, and D. J. Young, *Oxidation of Metals* **59**, 285 (2003).
43. R. Peraldi, D. Monceau, and B. Pieraggi, *Oxidation of Metals* **58**, 249 (2002).
44. S. N. Basu and J. W. Halloran, *Oxidation of Metals* **27**, 143 (1987).
45. A. Atkinson and R. I. Taylor, *High Temperatures-High Pressures* **14**, 571 (1982).
46. J. E. Castle and P. L. Surman, *Journal of Physical Chemistry-US* **71**, 4255 (1967).
47. A. G. Crouch and J. Robertson, *Acta Metallurgica et Materialia* **38**, 2567 (1990).
48. S. Mrowec, *Corrosion Science* **7**, 563 (1967).
49. T. Maruyama, N. Fukagai, M. Ueda, and K. Kawamura, *Materials Science Forum* **461–464**, 807 (2004).
50. C. Desgranges, N. Bertrand, K. Abbas, D. Monceau, and D. Poquillon, *Materials Science Forum* **461–464**, 481 (2004).